Research Article Vol. 32, No. 2 / 15 Jan 2024 / Optics Express 2147
Optics EXPRESS

Integrated polarization-free Bragg filters with subwavelength gratings for photonic sensing

DANIEL PIMBI,[1] MD BORHAN MIA,[1] NAFIZ JAIDYE,[2] ISHTIAQUE AHMED,[2] MEHEDI HASAN,[1] SYED Z. AHMED,[1] AND SANGSIK KIM[1,2,3,*]

[1]*Department of Electrical and Computer Engineering, Texas Tech University, Lubbock, Texas 79409, USA*
[2]*Department of Physics and Astronomy, Texas Tech University, Lubbock, Texas 79409, USA*
[3]*School of Electrical Engineering, Korea Advanced Institute of Science and Technology, Daejeon 34141, Republic of Korea*
[*]*sangsik.kim@kaist.ac.kr*

Abstract: We present polarization-free Bragg filters having subwavelength gratings (SWGs) in the lateral cladding region. This Bragg design expands modal fields toward upper cladding, resulting in enhanced light interaction with sensing analytes. Two device configurations are proposed and examined, one with index-matched coupling between transverse electric (TE) and transverse magnetic (TM) modes and the other one with hybrid-mode (HM) coupling. Both configurations introduce a strong coupling between two orthogonal modes (either TE-TM or HM_1-HM_2) and rotate the polarization of the input wave through Bragg reflection. The arrangements of SWGs help to achieve two configurations with different orthogonal modes, while expanding modal profiles toward the upper cladding region. Our proposed SWG-assisted Bragg gratings with polarization independency eliminate the need for a polarization controller and effectively tailor the modal properties, enhancing the potential of integrated photonic sensing applications.

1. Introduction

A Bragg grating is a periodic structure capable of modulating the phase along the wave propagation [1–3]. In integrated photonics, a grating can be realized by either corrugating the waveguide [3,4] or periodically segmenting waveguide blocks [5,6] such that the spatial phase modulation causes destructive interference inside the gratings and reflects back the input light. The wavelength of this Bragg reflection corresponds to the forbidden region of the photonic bandgap. Hence, Bragg gratings function as wavelength-selective notch filters and serve as fundamental components in many optical systems [7,8]. One of the applications of a Bragg grating is an optical sensing [9,10], which is widely explored in integrated photonics [9–12]. Integrated photonic sensors allow the highly sensitive and selective detection of biological species and gases in real time without labels or dyes [9–14]; thus, they have been explored for rapid point-to-care clinical diagnosis [14], greenhouse gas monitoring [15], and food safety control [16].

The integrated photonic sensing principle is based on either resonance shift or power absorption variation due to the interaction between the waveguide's evanescent field and the analytes [14,17]. The surrounding analytes or gases change the propagation constants and/or loss of the guided mode, which would shift the resonance wavelength and/or reduce the output transmission power. By mapping and analyzing these measured data, one can easily detect the presence or quantify the concentration of the target species. For example, the phase variation of photonic Mach-Zehnder interferometers (MZIs) causes the wavelength shift for constructive and destructive interferences, directly converting the phase shift to optical power variation [18,19]. Similarly, transmission dips in Bragg gratings [20–26] and ring-resonators [27–29] also shift as per cladding index changes via analytes. Among these widely known integrated photonic sensor configurations (i.e.,

#504043 https://doi.org/10.1364/OE.504043
Journal © 2024 Received 24 Aug 2023; revised 13 Nov 2023; accepted 17 Nov 2023; published 8 Jan 2024

Optics EXPRESS

MZIs, ring-resonators, and Bragg gratings), the Bragg grating configuration can exhibit almost a single transmission dip in the spectra, while the other MZI and ring-resonator configurations show multiple resonance dips. A Bragg grating also has multiple transmission dips with 2^{nd}, 3^{rd}, and higher grating orders, but their spectral location is relatively away from its 1^{st} order grating transmission dip. In other words, the free-spectral-ranges (FSRs) of MZI and ring-resonator configurations are much narrower than that of a Bragg grating, limiting the sensing range of MZI and ring-resonator configurations. For example, typical FSRs of MZIs and ring-resonators are in a scale of a few nanometers in wavelength (at telecommunication band), while that of Bragg grating is in a scale of hundreds of nanometers. One may optimize the bending radius of a ring-resonator and the interference length of MZI to increase the FSRs, but these approaches will cause additional losses in the system and eventually be limited. In this context, the Bragg grating configuration is almost free from the range of sensing distinguishability.

Recently, subwavelength gratings (SWGs) have gained attention among researchers as potential sensors due to their ability to enhance light-matter interaction with surrounding analytes [10,17]. SWGs provide additional degree of freedoms for engineering the refractive indices and anisotropy of composite materials [10,30–33], which can lead to engineering modal confinement [34], skin-depth [35], and dielectric perturbations [36,37]. Utilizing these SWG properties, many components-level integrated photonic devices have been advanced, for example, fiber-to-chip couplers [38,39], polarization beam splitters [40–42], polarization splitter and rotators [43,44], delay lines [45,46], graded-index lenses [47,48], and so on. Specific to sensing applications, researchers mainly focused on increasing the device sensitivity and minimizing the intrinsic limit of detection (iLoD) by utilizing SWGs in both resonant and interferometric schemes [10]. For example, an SWG waveguide sensor was demonstrated to maximize the waveguide bulk sensitivity near unity by optimizing the grating duty cycle of the SWG waveguide [17]. A lower iLoD is also resolvable by utilizing an SWG-based Bragg grating sensor, achieving an iLoD of $5.1\text{x}10^{-5}$ RIU that is one order of magnitude lower than other resonant sensors [20]. A bimodal SWG waveguide-based interferometric sensor has also been shown to improve the total device sensitivity up to 2270 nm/RIU [49].

However, all the previous integrated photonic sensor schemes are sensitive to the polarization status and typically operate at a single polarization. This means that the system requires a polarization controller at some point in the setup, potentially necessitating bulky components. More fundamentally, polarization uncertainty and instability are not desired in sensors since they cause power variations or resonance shifts. Minor variations in the input polarization state could lead to systematic errors, uncertainties, or a failure to detect analytes. Thus, having a polarization-free photonic sensing scheme is important. However, to our knowledge, all the previous integrated photonic sensing works operated at a single polarization [9–29].

The reason for the polarization sensitivity is due to the asymmetric aspect ratio of the waveguide cross-section [50,51]. A typical photonic waveguide has an asymmetric height-to-width ratio, having a larger width than height. This is because of an easier etching during the chip fabrication process. However, this cross-section asymmetry induces different effective indices for different polarizations, resulting in different output signals for almost every photonic component, including sensors. For Bragg gratings, a couple of approaches have been proposed to realize polarization-insensitive Bragg filters, such as TE/TM index-matching [52–55] and polarization-rotating Bragg [56, 57] methods. Unfortunately, these designs cannot be directly utilized for sensing applications since they had silicon oxide (SiO_2) upper cladding. Recently, the concept of polarization-independent and rotation Bragg filter using cladding asymmetry was proposed, demonstrating it with air cladding [50]. Since the cladding asymmetry was demonstrated with air cladding, the exposed waveguide can easily interact with analytes, making the scheme potentially applicable for polarization-free photonic sensors. Still, the design itself is not ideal for a sensing

Optics EXPRESS

application due to the short skin-depth of the evanescent field in the upper cladding, limiting its sensitivity and iLoD.

In this paper, we propose polarization-free integrated photonic sensing schemes based on Bragg gratings with SWG claddings. The polarization independence is achieved by breaking the vertical symmetry via analyte cladding. For achieving polarization independency, two schemes are proposed (index-matched and hybrid-mode), both having two different orthogonal mode sets. The device sensitivity of our polarization-free photonic sensors is enhanced by SWG claddings. Such SWG-assisted Bragg filters can efficiently tailor the modal field to extend its evanescent field, which increases the interaction with the surrounding analytes. We experimentally demonstrated both schemes of polarization-free Bragg filters on a silicon-on-insulator (SOI) platform via a single etching process. The polarization-free characteristics are also examined while quantifying their sensitivity and iLoD. In the following sections, we present two schemes for achieving polarization-free Bragg filters, along with their design concepts, show numerical results, and experimentally demonstrate polarization-free Bragg responses using different index-matched liquid claddings. We then analyze both devices by quantifying the total device sensitivity and iLoD and compare and discuss the results.

2. Design and analysis

2.1. Bragg grating biosensor based on subwavelength gratings

Generally, periodic gratings exhibit three operating regimes, namely the diffraction, reflection, and subwavelength regimes, depending on the scale difference between the periodic pitch (i.e., grating period) and the operating wavelength [10,33]. The diffraction regime operates at a wavelength smaller than the pitch, interfacing the guided and radiation modes, for example, in fiber-to-chip grating couplers [38,39]. In the reflection regime, the gratings operate at a wavelength near twice the grating period (i.e., Bragg grating) [3,50]. The subwavelength regime arises when the operating wavelength is considerably longer than the periodicity [33–37]. This regime effectively suppresses diffraction and reflection, making the gratings behave as an equivalent homogeneous metamaterial with dielectric permittivity governed by the effective medium theory (EMT) [36]. The gratings in this regime are referred to as subwavelength gratings (SWGs) and are extensively utilized to advance on-chip light manipulation and control [10]. One kind of SWG waveguide, where SWGs are arrayed in parallel to the wave propagation direction as in Fig. 1, is called an extreme skin-depth (eskid) waveguide since it can control the evanescent wave skin-depth of the TE mode due to the SWG's anisotropy in the cladding [36]. In the eskid configuration, the mode size of TM can be largely expanded, also introducing a larger birefringence between the TE and TM modes. In previous works, this large birefringence characteristic of the eskid waveguide has been applied to enhance the polarization beam splitter performances [40–44]. Here, we employed this eskid waveguide configuration to expand the interactive modal area with its large birefringence while achieving a polarization-free Bragg response with its cladding asymmetry for an efficient integrated photonic sensor.

Figures 1(a) and 1(c) show the top views of the proposed polarization-free photonic Bragg gratings with SWG claddings. Figure 1(a) is designed to match the effective refractive indices of TE and TM modes, and Fig. 1(c) is designed to introduce hybrid modes (HM). Both configurations are designed on an SOI platform with a 220 nm thick Si (blue color) on top of a 2 μm thick buried oxide layer (gray color). Upper cladding is opened with air and used to create the vertical asymmetry for the polarization-independent Bragg filtering. The key difference between Figs. 1(a) and 1(c) is the gap symmetry and asymmetry between the core and SWG claddings. In the index-matched design in Fig. 1(a), the cross-section of each segment is laterally (x-axis) symmetric, having the same gap size as g_0. This will exhibit distinctive TE_0 and TM_0 modes, as shown in Fig. 1(b). Then, the Bragg gratings in the propagation direction (z-axis) are introduced by shifting the center position of each grating segment. On the other hand, in the hybrid mode

Optics EXPRESS

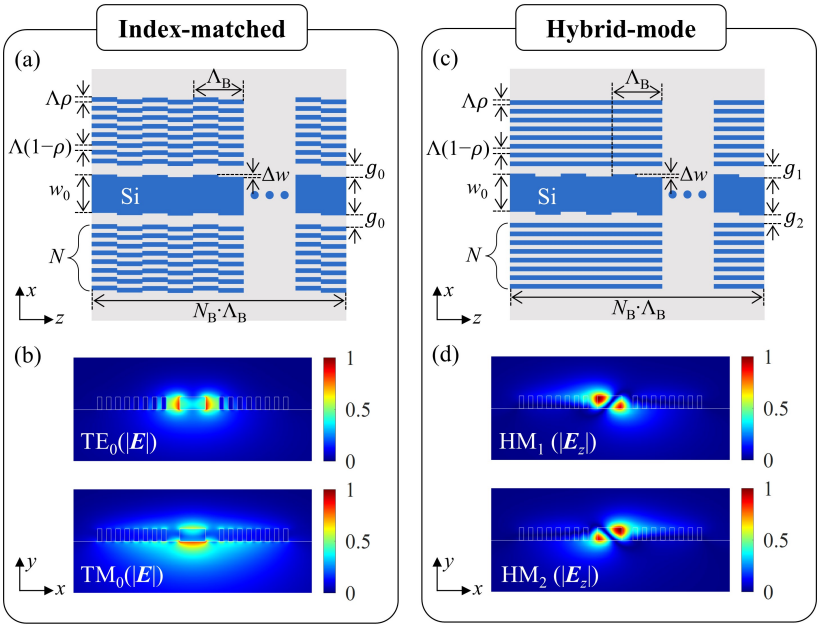

Fig. 1. Top views of the proposed polarization-free Bragg grating sensors with SWG cladding: (a) index-matched and (c) hybrid-mode configurations. The index-matched configuration is realized using a core width w_0 = 280 nm with symmetric gap size g_0 = 150 nm to the lateral SWG claddings, a corrugation depth Δw = 20 nm, and a Bragg periodicity Λ_B = 500–560 nm with number of Bragg periods N_B = 100–500. The SWG claddings have grating period Λ = 100 nm, filling fraction ρ = 0.5, and number of layers N = 8. The hybrid configuration has the same geometric parameters as the index-matched configuration except having asymmetric gaps g_1 = 120 nm and g_2 = 100 nm. (b) is the normalized electric field profiles ($|\boldsymbol{E}|$) of TE_0 (above) and TM_0 (bottom) modes at the index-matching condition. (d) shows the normalized electric field profiles ($|\boldsymbol{E}_z|$) of HM_1 (above) and HM_2 (bottom) at mode hybridization.

design in Fig. 1(c), the SWG lines are fixed while shifting the center position of the waveguide core, having the asymmetric gaps g_1 and g_2. The asymmetry introduced by these gaps results in two orthogonal hybrid modes (HM_1 and HM_2), as plotted in Fig. 1(d). Since these two modes are coupled, they will exhibit avoided mode crossing during the parameter sweep. We also expect the hybrid scheme will have a lower scattering loss than the index-matched design due to its fewer discrete points at the grating interfaces.

Regarding the detailed parameters, we used SWG claddings with a grating period Λ = 100 nm and a filling fraction ρ = 0.5 to satisfy the subwavelength regime, i.e., $\Lambda << \lambda/(2n_{eff})$, where λ and n_{eff} are the free-space wavelength and effective index of the guided mode, respectively. We limited the number of layers to N = 8 to allow single-mode operation while extending the modal area. We fixed the corrugation depth to Δw = 20 nm, which could cause a strong enough coupling coefficient between TE_0 and TM_0 or HM_1 and HM_2 modes in our Bragg schemes. This corrugation depth is the key parameter that determines the coupling coefficient, thus the achievable extinction ratio per number of Bragg periods (or unit length) and the bandwidth of the Bragg response. The Bragg periodicity determines the center wavelength of the Bragg reflection, and it is in the range of Λ_B = 500–560 nm for our schemes. The number of Bragg periods will decide the achievable Bragg extinction ratio, and we examined N_B = 100–500, which corresponds to the device lengths of approximately 50 – 280 μm range. We set the offset gap sizes between

Optics EXPRESS

the core and SWG claddings as $g_0 = 150$ nm, $g_1 = 120$ nm, and $g_2 = 100$ nm, such that those SWG perturbations do not cause significant scattering losses in real experiments.

We then ran the modal simulations tracking the effective refractive indices of both orthogonal modes (TE_0 and TM_0 for index-matched design and HM_1 and HM_2 for hybrid-mode design) while varying the core width and fixing the other parameters as noted above. Figure 2(a) shows the modal effective refractive indices n_{eff} of TE_0 (blue) and TM_0 (yellow) modes as a function of the core width w_0. The free space wavelength is 1550 nm. In Fig. 2(a), both indices n_{TE0} and n_{TM0} are matched near $w_0 \approx 277$ nm. Since the fabrication imperfection errors could be in the range of ±5 nm, we rounded the core width to $w_0 = 280$ nm. Then, to predict the Bragg wavelength and its corresponding Bragg periodicity Λ_B, we re-simulated the effective refractive indices as a function of wavelength while fixing the other geometric parameters ($w_0 = 280$ nm). Figure 2(b) shows the effective refractive indices as a function of wavelength for TE_0 (blue) and TM_0 (yellow). The wavelength for index-matching is shifted to ≈1573 nm, due to our approximation with $w_0 = 280$ nm. The orange line represents the average effective index $n_{\text{avg}} = (n_{\text{TE0}} + n_{\text{TM0}})/2$, which determines the polarization-rotating Bragg wavelength [50,57,58]. Similarly, in Figs. 2(c) and 2(d), we simulated the n_{eff} of the hybrid configuration (HM_1 and HM_2) as a function of w_0 and wavelength ($w_0 = 270$ nm), respectively. In these cases, avoided mode crossing is observed, which indicates the coupling between HM_1 and HM_2.

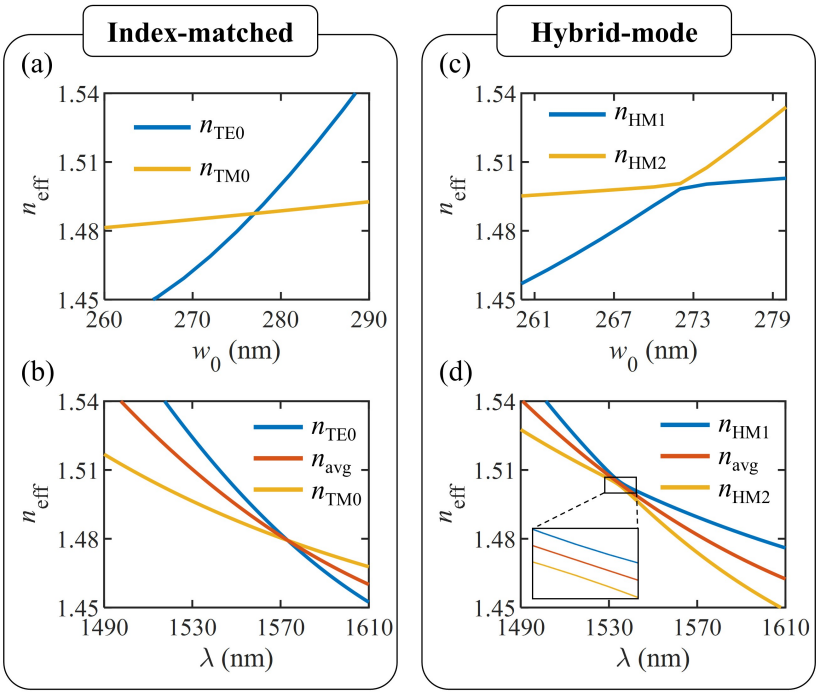

Fig. 2. (a) and (c) are the simulated effective refractive indices (n_{TE0} and n_{TM0}) of the index-matched and (n_{HM1} and n_{HM2}) of the hybrid-mode configurations, respectively, as a function of the core width w_0. (b) and (d) show the re-simulated effective refractive indices as a function of wavelength while fixing the core width to $w_0 = 280$ nm (b) and $w_0 = 270$ nm (d). The orange lines represent the average effective index n_{avg} between n_{TE0} (n_{HM1}) blue and n_{TM0} (n_{HM2}) yellow, respectively.

Regardless of either configuration, due to upper cladding asymmetry, both configurations could introduce a strong coupling between the two orthogonal modes (TE_0 and TM_0 for index-matched

Optics EXPRESS

design and HM_1 and HM_2 for hybrid design). This will require the Bragg conditions to be satisfied between the two orthogonal modes, i.e., polarization-rotating Bragg response. In other words, the phase-matching condition will fulfill between the two opposite propagating polarization modes and the grating phase, i.e., the Bragg condition follows [50,56]:

$$\lambda_B = (n_{TE0} + n_{TM0})\Lambda_B = 2n_{avg}\Lambda_B \tag{1}$$

where λ_B is the Bragg wavelength. Note that the Bragg wavelength is determined by the average indices of the two orthogonal polarizations. At this polarization-rotating Bragg condition, the input polarization is rotated to the other orthogonal polarization and then reflected back in the opposite direction. So, it can be viewed as a combination of Bragg reflection and polarization rotation. Since the Bragg condition in Eq. (1) happens at the average of two modes, from the spectral viewpoint, the condition is independent of input polarization status, i.e., polarization-independent [50].

Using the simulated n_{eff} data in Fig. 2 and Eq. (1), we can estimate the Bragg wavelength λ_B associated with its Bragg period Λ_B [note that n_{avg} in Eq. (1) is also dependent on λ]. Figures 3(a) and 3(c) show the λ_B estimations for each index-matched and hybrid configuration, where we choose Λ_B = 500–560 nm to ensure λ_B appears near the telecommunication band. Our λ_B estimations match well with both numerical and experimental results (which will be shown later). Having the λ_B predictions, we examined the performance of each Bragg configuration using an eigenmode expansion (EME) solver available in Ansys Lumerical software [59]. We chose the EME method since the simulation time does not scale with the number of periods (or propagation length) in a periodic structure like our Bragg gratings. Each EME simulation returns the scattering matrices (s-matrices) data containing the transmission and reflection coefficients, which we used for computing the transmission and reflection spectra. Figures 3(b) and 3(d) show the EME simulated transmission spectra for the two proposed configurations, respectively. The blue-solid and yellow-dashed lines represent the cases of TE_0 (HM_1) and TM_0 (HM_2) input modes, respectively. In all cases, the Bragg periodicity and the number of periods are set to Λ_B = 500 nm and N_B = 300, respectively. The upper cladding is opened with air (i.e., the upper cladding index is n_{clad} = 1.00). Notice that, in both configurations [Figs. 3(b) and 3(d)], regardless of input polarization status, either TE_0 (HM_1) or TM_0 (HM_2) mode, the spectral responses match perfectly (i.e., blue-solid and yellow-dashed lines match exactly), having the same central Bragg wavelength, extinction ratio, and bandwidth; i.e., perfect polarization-independency. The central λ_B of EME simulated transmission spectra also agree very well with their theoretical estimations [the case of Λ_B = 500 nm is marked in Figs. 3(a) and 3(c)]. We also ran EME simulations while varying the Bragg period Λ_B±20 nm, then the λ_B shift is approximately ±34(36) nm for the index-matched and hybrid configurations, respectively. This shift rate also matches well with the λ_B estimates in Figs. 3(a) and 3(c), where the graph slopes of the λ_B shift as per Λ_B is approximately $\lambda_B/\Lambda_B \approx 1.71$ and 1.77 , respectively. In addition, using the simulated transmission spectra and total device length, the total coupling coefficients can be directly calculated from the coupled-mode theory (CMT) formula for the peak power reflectivity $R_{peak} = \tanh^2(\kappa L)$ [1,3,5]. Where $R_{peak} = 1 - T_{dip}$, where T_{dip} defining the transmission power dip at the Bragg wavelength. The total coupling coefficient κ can be then simplified as [1,3,5]:

$$\kappa = \frac{1}{L}\tanh^{-1}\left(\sqrt{1 - T_{dip}}\right). \tag{2}$$

This κ describes the amount of reflection per unit length, i.e., how quickly the forwarding wave (input mode) transfers its power into the reflected mode. Based on Eq. (2), we estimate the Bragg coupling coefficients $\kappa \approx 3.1\text{x}10^4$ m^{-1} and $2.8\text{x}10^4$ m^{-1} for the index-matched and hybrid-mode configurations, respectively.

Optics EXPRESS

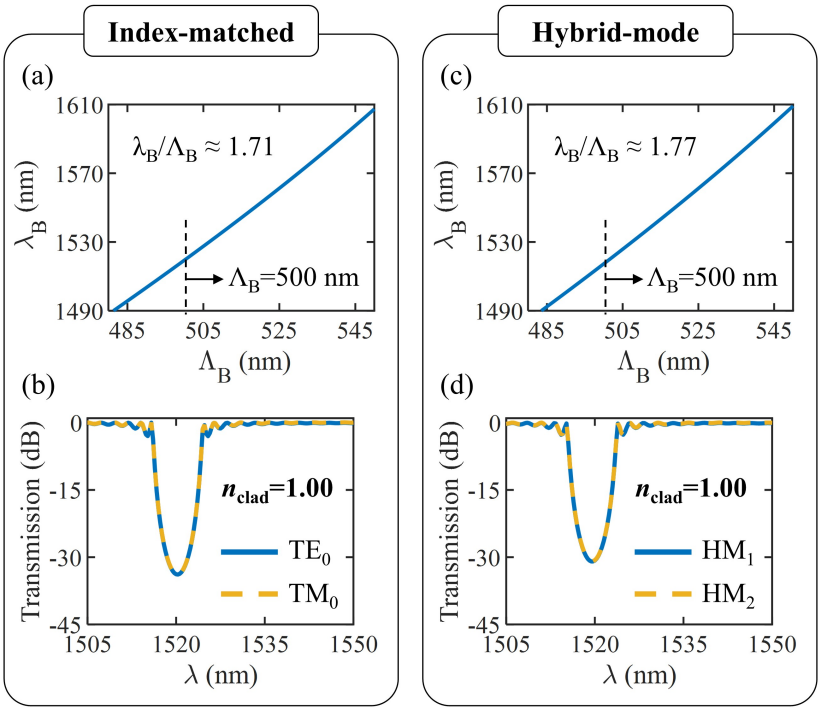

Fig. 3. (a) and (c) are the theoretical estimates of Bragg wavelength λ_B as a function of Bragg period Λ_B for index-matched and hybrid-mode configurations using Eq. (1). (b) and (d) show the numerically simulated transmission spectra of TE_0/HM_1 (blue solid) and TM_0/HM_2 (yellow dashed) input modes, respectively. The Bragg period Λ_B = 500 nm, the number of periods N_B = 300, the upper cladding index n_{clad} = 1.00, and the other parameters are fixed and given in Fig. 1.

2.2. *Device sensitivity*

The waveguide sensitivity is a measure of the variations in the effective index of the guided light due to physical changes in the analyte. The changes in the analyte can be quantified using either bulk or surface sensitivity [17,20,21]. In general, the bulk sensitivity is defined as the ratio of the changes in the effective index to the cladding index due to analytes ($\partial n_{eff}/\partial n_{clad}$) [17]. Whereas, the surface sensitivity is a ratio of the changes in the effective index to the thickness t of the absorbed analyte layer ($\partial n_{eff}/\partial t$) [17]. Here, we will focus on the quantity related to the bulk sensitivity. From the practical viewpoint, directly quantifying the bulk sensitivity is difficult, and there could be limiting factors when mapping the signals. Thus, the device's overall sensitivity, including bulk and architecture sensitivities, is widely utilized [20]. In the case of sensors like Bragg gratings, the effective index is mapped to the wavelength shift, defined by the architecture sensitivity $\partial\lambda_B/\partial n_{eff}$ [20]. Thus, as a whole, to quantify the overall sensitivity of the wavelength-shift type sensors, the total sensitivity S is defined as the product of the architecture sensitivity and the bulk sensitivity, as the following [20]:

$$S = \frac{\partial \lambda_B}{\partial n_{eff}} \frac{\partial n_{eff}}{\partial n_{clad}} = \frac{\partial \lambda_B}{\partial n_{clad}}. \tag{3}$$

Since the product of bulk and architecture sensitivities cancels out the ∂n_{eff}, the total sensitivity S is equivalent to the slope of the wavelength shift per cladding refractive index change. To estimate the sensitivity S of our proposed polarization-free Bragg gratings, we extracted the

Optics EXPRESS

wavelength shifts by re-simulating the transmission spectra while varying the upper-cladding refractive indices. Figures 4(a) and 4(c) show the EME simulated transmission spectra of TE_0/HM_1 (above) and TM_0/HM_2 (bottom) inputs with different cladding indices: n_{clad} = 1.30 (purple) and 1.35 (green). As expected, the transmission spectra are redshifted as the cladding refractive index increases. Still, regardless of the input polarization, the Bragg responses in the spectrum are the same for each case, which is the most important feature of our polarization-free Bragg grating sensing schemes. Figures 4(b) and 4(d) show the extracted Bragg wavelengths of TE_0/HM_1 (blue solid) and TM_0/HM_2 (yellow dashed) as a function of the upper cladding index n_{clad} using EME transmission spectra. Applying Eq. (3), the device sensitivities are approximately $S \approx 260$ nm/RIU and $S \approx 278$ nm/RIU for the index-matched and hybrid designs, respectively.

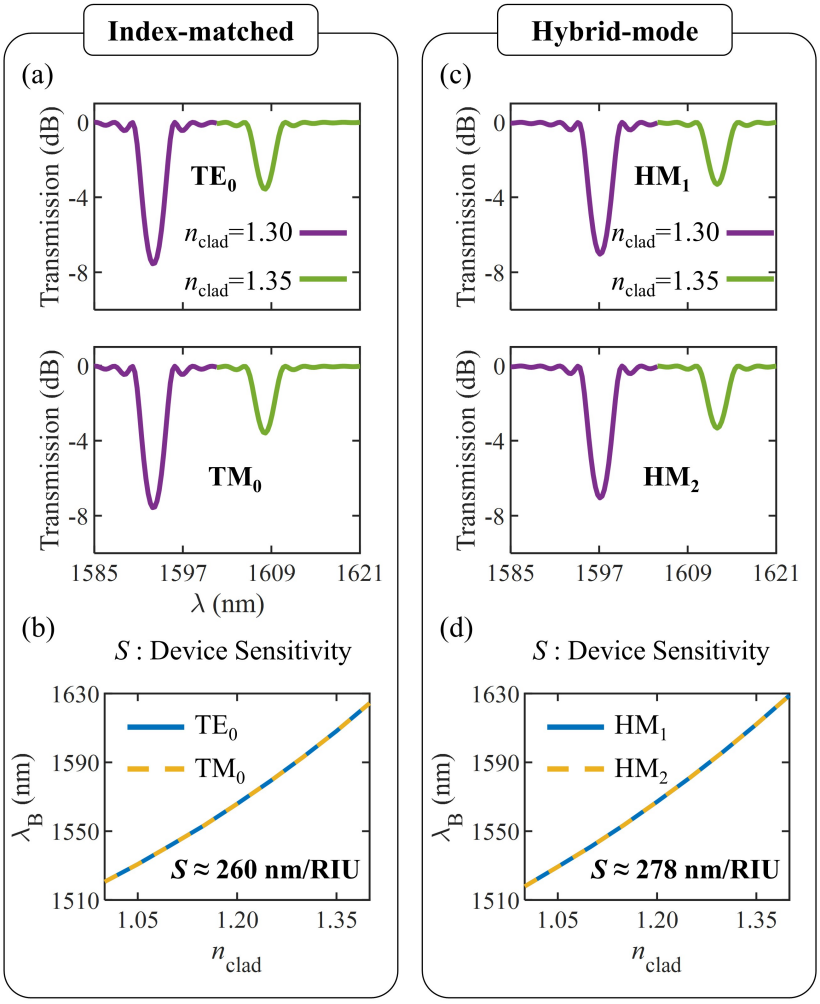

Fig. 4. (a) and (c) are the simulated transmission spectra of TE_0/HM_1 (above) and TM_0/HM_2 (bottom) input modes for different upper cladding indices n_{clad} = 1.30 (purple) and 1.35 (green). (b) and (d) show the extracted Bragg wavelength λ_B of TE_0/HM_1 (blue solid) and TM_0/HM_2 (yellow dashed) as a function of n_{clad}. Using Eq. (3), we estimated total device sensitivities $S \approx 260$ nm/RIU and $S \approx 278$ nm/RIU for the two configurations. The geometric parameters are the same as in Fig. 3.

Optics EXPRESS

Another important figure of merit for integrated photonic sensors is the iLoD. It describes the minimum detectable refractive index unit change by the sensor [17,20]. For Bragg structures, since we are observing the refractive index change via wavelength shift, it is typically compared by 3 dB bandwidth of Bragg spectrum per sensitivity (assuming that 3 dB bandwidth is reasonably detectable in the system). Thus, iLoD follows [20],

$$\text{iLoD} = \frac{\Delta\lambda_{3\text{dB}}}{S} \tag{4}$$

where $\Delta\lambda_{3\text{dB}}$ is the 3 dB bandwidth [or full width at half maximum (FWHM) bandwidth]. Since our $\Delta\lambda_{3\text{dB}}$ is ≈3.3 nm for the current design (Figs. 4), we estimated the intrinsic limit of detection iLoD ≈ 12x10^{-3} RIU for the index-matched and hybrid configurations. Note that the iLoD heavily depends on the bandwidth of the Bragg filter. In our current design, we didn't aim to achieve a narrow bandwidth filter that is ideal for a low-iLoD sensor, but it should be achievable by reducing the corrugation depth Δw and minimizing the perturbation strength in the filter, in trade of the device length and extinction ratio.

3. Experiment

3.1. Fabrication and experimental characterization

To confirm the concept of polarization-free Bragg sensors, we fabricated our Bragg devices on an SOI wafer. The gratings were patterned using electron beam lithography and followed typical SOI processes [36]. Two sets of devices were fabricated for each configuration, one with TE and the other with TM grating couplers. This ensures the polarization status during each experimental characterization. The grating coupler first couples the fiber mode to the strip waveguide mode of a specific polarization and then adiabatically convert it to the eskid mode, selectively exciting either TE or TM. The same approach also makes sure of the selective excitation of two orthogonal hybrid modes, HM_1 or HM_2. Figure 5(a) shows the scanning electron microscope (SEM) image of the fabricated device set, including input and output grating couplers. Each section shows 1) strip-to-eskid waveguide transitions, 2) straight eskid waveguides with the core size of w_0 = 450 nm, and 3) adiabatic mode transitions, where core w_0 is adiabatically tapered from 450 nm to 270-280 nm over a propagation length of 40 μm. The designed Bragg gratings are located in the middle of the scheme (indicated by the yellow arrow). Figures 5(b) and 5(c) are the zoomed-in SEM images showing the Bragg grating regions of 5(b) index-matched and 5(c) hybrid-mode cases, respectively. We experimentally characterized our Bragg gratings using a custom-built grating coupler setup with a tunable laser source and an optical power meter. We used an external polarization controller that was connected after the tunable laser source to control the polarization state of the input light. Calibration devices with only the grating couplers and strip waveguides were also fabricated and used to normalize the spectra.

Figures 5(d) and 5(e) show the experimentally characterized transmission spectra of index-matched and hybrid configurations, respectively. The blue solid and orange dashed lines represent TE_0 (HM_1) and TM_0 (HM_2) excitations, respectively. As a first characterization, these devices were measured under air cladding, which corresponds to the simulated results obtained in Figs. 3(b) and 3(d), respectively. Notably, the central Bragg wavelength λ_B of transmission dips for TE_0 (HM_1) and TM_0 (HM_2) excitations are almost identical, having the polarization dependency of 0.25 nm and 0.57 nm for index-matched and hybrid-mode configurations, respectively; these results clearly confirm our Bragg gratings' polarization independency. Note that, for characterization purposes, different polarization measurements were performed at different chips but with the same design. Thus, we consider even such a low polarization-dependency to be from fabrication imperfections between the chips. Compared to simulated results in Figs. 3(b) and 3(d), the Bragg wavelengths are blue-shifted by ≈7.4 and ≈15.6 nm, probably due to fabrication imperfections and wafer non-uniformity. The characterized FWHMs of index-matched and hybrid

Optics EXPRESS

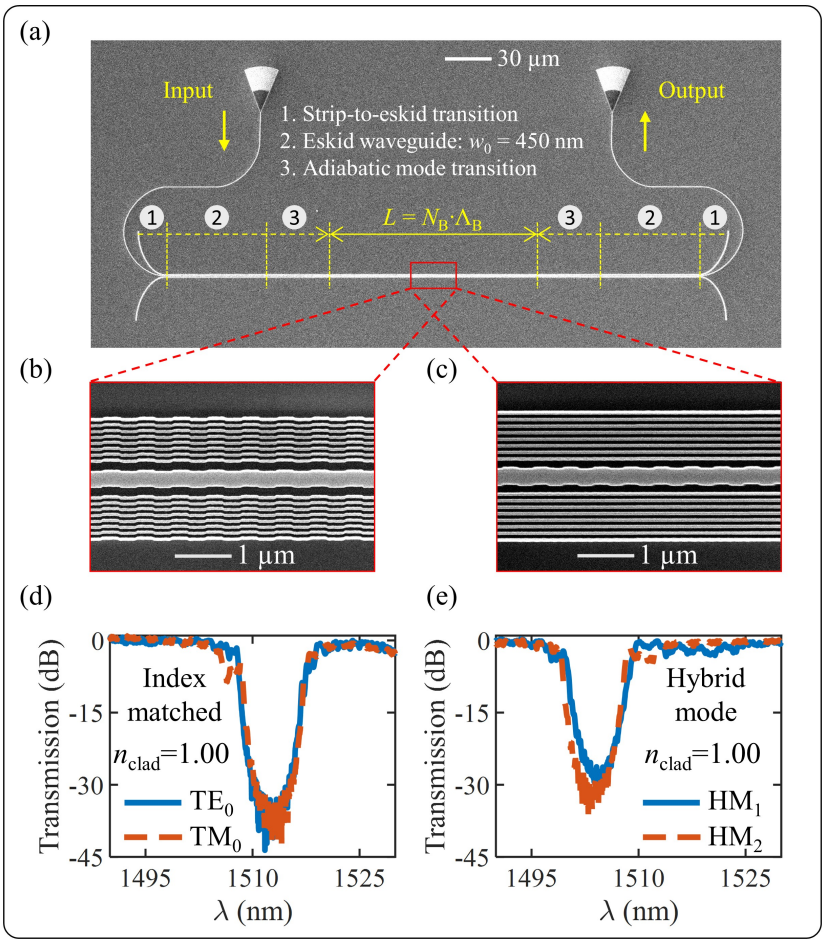

Fig. 5. (a) Scanning electron microscope image of the fabricated device set, showing input and output grating couplers, strip-to-eskid waveguide transitions, eskid waveguides with w_0 = 450 nm, adiabatic mode transitions (where w_0 is tapered from 270-280 nm to a core width of 450 nm over a propagation length of 40 μm), and Bragg grating region in the middle of the scheme (indicated by the yellow arrow). (b) and (c) are zoomed-in images showing the Bragg grating region of (b) index-matched and (c) hybrid-mode configurations. (d) and (e) are their experimentally characterized transmission spectra of TE_0 /HM_1 (blue solid) and TM_0/HM_2 (orange dashed) excitations corresponding to the simulated results in Figs. 3(b) and 3(d), respectively.

Optics EXPRESS

configurations are ≈9.6 nm and ≈9.0 nm, respectively, which are slightly broader compared to those from simulations [≈8.2 nm and ≈8.1 nm from Figs. 3(b) and 3(d), respectively]. The FWHM bandwidth critically depends on the perturbation between each cross-section introduced by Δw, and we suspect the fabricated Δw is slightly wider than the designed one. The extinction ratios of each configuration are ≈ 36.8 ± 0.43 dB and ≈ 30.4 ± 0.83 dB, which are slightly higher than simulated results, also can be due to a larger Δw consistent with the bandwidth difference. Furthermore, using Eq. (2), we can extract the experimental coupling coefficients of index-matched and hybrid configurations as ≈ $3.3\text{x}10^4$ m^{-1} and ≈ $2.8\text{x}10^4$ m^{-1}, respectively, again attesting a larger Δw. Still, regardless of fabrication imperfections and these differences between numerical and experimental results, both configurations show highly tolerant polarization independency, which is the main feature of our proposed schemes. It is worth noting that our devices can also be fabricated with larger feature sizes that are compatible with the commercially available silicon photonic complementary metal–oxide semiconductor (CMOS) processes [60].

3.2. Polarization-free sensitivity characterization

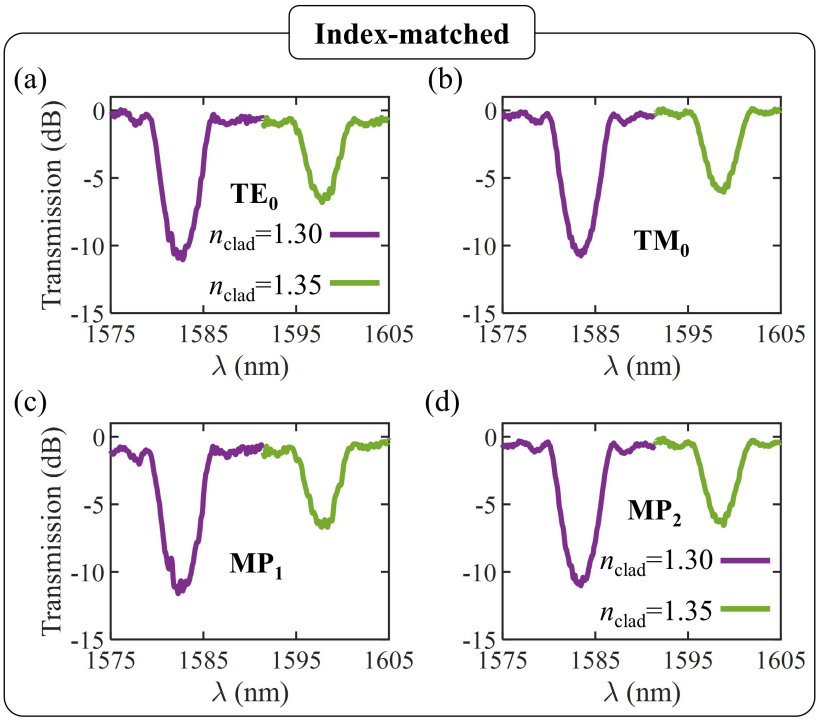

Fig. 6. (a) and (b) are the experimentally characterized transmission spectra of TE_0 and TM_0 excitations for different upper cladding indices n_{clad} = 1.30 (purple) and n_{clad} = 1.35 (green), which correspond to the simulated results in Fig. 4(a). (c) and (d) show similar experimentally characterized transmission spectra with (c) mixed polarization (MP_1, +45°) and (d) (MP_2, -45°) excitations.

To show the polarization-free sensing capabilities of the two configurations, we covered our devices with index-matching fluids (Series AAA, Cargille Laboratories) and tested their polarization insensitivities while varying the input polarization status. Figures 6 and 7 show the experimentally characterized transmission spectra of the index-matched and hybrid configurations, respectively. Two different index-matching fluids are used: n_{clad} = 1.30 (purple) and 1.35 (green).

Optics EXPRESS

In each figure, the input polarization status is varied and measured, exciting four different polarizations: (a) TE_0 (HM_1), (b) TM_0 (HM_2), (c) Mixed polarization 1 (MP_1, +45°), and (d) MP_2 (-45°). Among these four different polarization characterizations, the difference in Bragg wavelengths is only <0.69 nm in Fig. 6 and <0.11 nm in Fig. 7, respectively, and their extinction ratio differences are <0.82 dB and <0.66 dB. Note that we fabricated identical designs on different chips, each having TE or TM grating couplers. We assert these observed differences are likely attributed to variations in grating couplers and potential uncertainties in characterization.

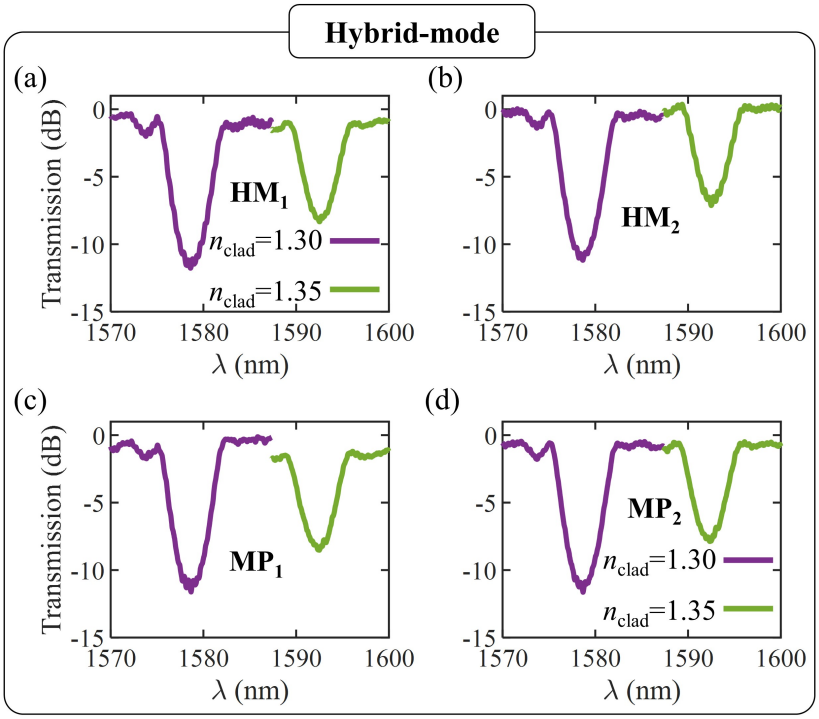

Fig. 7. (a) and (b) are the experimentally characterized transmission spectra of HM_1 and HM_2 excitations for different upper cladding indices n_{clad} = 1.30 (purple) and n_{clad} = 1.35 (green), which correspond to the simulated results in Fig. 4(c). (c) and (d) show similar experimentally characterized transmission spectra with (c) mixed polarization (MP_1, +45°) and (d) (MP_2, -45°) excitations.

The measured results in Figs. 6 and 7 correspond to the simulated results in Figs. 4(a) and 4(c). Similar to their air cladding results in Fig. 5, the experimentally characterized Bragg wavelengths are blue-shifted by ≈10.7 and ≈18.4 nm compared to their corresponding simulation results. The degree of blue shift compared to simulation data is almost identical among different cladding indices' results, suggesting the devices' overall sensitivity closely matches the simulated results. Quantitatively, our experimental data show the overall sensitivity of $S \approx 250$ nm/RIU and iLoD $\approx 13\text{x}10^{-3}$ RIU with the $\Delta\lambda_{3dB} \approx 3.4$ nm. From these experiments, we could conclude that our fabricated devices' sensitivity and intrinsic limit of detection reasonably agree well with our numerical designs while preserving their robust polarization-free characteristics (even though there are spectral shifts due to fabrication imperfections, mainly due to Δw). In contrast to most approaches that rely on a single polarization mode operation requiring additional polarization controlling components [9–29], our devices offer the distinct advantage of being polarization-free, not necessitating polarization controllers.

Optics EXPRESS

4. Conclusion

In this work, we have proposed and experimentally demonstrated the concept of polarization-free Bragg filters for integrated photonic sensing applications. The SWG claddings are integrated with Bragg schemes, expanding the modal overlap with sensing analytes. Two different configurations with index-matching and hybrid modes are proposed and compared, both exhibiting highly tolerant polarization independency. Their polarization-free characteristics were realized by introducing vertical asymmetry, which enables strong coupling between TE_0 and TM_0 modes for index-matched design and HM_1 and HM_2 modes for hybrid design. Thanks to the inherent ability of SWGs to tailor the modal properties and evanescent waves, we could achieve a high device sensitivity with the proposed polarization-free Bragg sensors. We report experimental device sensitivities of $\approx$ 245 nm/RIU and $\approx$ 254 nm/RIU for index-matched and hybrid configurations, respectively, which are quite close to simulated results. Both configurations achieved iLoD $\approx 13\text{x}10^{-3}$ RIU. With further parameter optimization and slight tuning of our device schemes, we expect the device's sensitivity and intrinsic limit of detection to be improved. For example, each of our schemes can be directly integrated into phase-shifted Bragg grating devices to aim for a narrow bandwidth passband resonance that is crucial for achieving a low iLoD. Furthermore, using the properties of SWGs to increase the modal area of interaction with the sensing analytes, our schemes can offer better design flexibility while improving the sensitivity and detection of specific biomarkers or pathogens in real biosensing applications. Our polarization-free sensing schemes offer a robust solution to the challenges of polarization uncertainty prevalent in nearly all optical systems influenced by environmental factors. This approach, in general, can be expanded further to other absorption-based sensing techniques and spectral ranges, including mid-infrared sensing. By eliminating the need for polarization controllers, our schemes can both miniaturize the system and reduce costs while mitigating polarization uncertainty. With the systematic integration of on-chip light sources and detectors, our polarization-free Bragg scheme is expected to support the transition from lab-scale photonic sensing technology to practical and portable real-world field applications.

Funding. National Science Foundation (2144568); U.S. Department of Energy (DE-NA-0003525); National Research Foundation of Korea (2023M3K5A1094806, RS-2023-00210997); Korea Advanced Institute of Science and Technology (G04220043).

Acknowledgments. This work was performed, in part, at the Center for Integrated Nanotechnologies (CINT), an Office of Science User Facility operated for the U.S. Department of Energy Office of Science by Los Alamos National Laboratory and Sandia National Laboratories.

Disclosures. The authors declare no conflicts of interest.

Data Availability. Data underlying the results presented in this paper are not publicly available at this time but may be obtained from the authors upon reasonable request.

References

1. A. Yariv and P. Yeh, *Photonics: Optical Electronics in Modern Communications* (Oxford University Press, 2007).
2. J. Buus, M.-C. Amann, and D. J. Blumenthal, *Tunable laser diodes and related optical sources* (John Wiley & Sons, 2005).
3. X. Wang, "Silicon photonic waveguide Bragg gratings," Ph.D. thesis, University of British Columbia (2013).
4. D. Oser, D. Pérez-Galacho, C. Alonso-Ramos, *et al.*, "Subwavelength engineering and asymmetry: two efficient tools for sub-nanometer-bandwidth silicon Bragg filters," Opt. Lett. **43**(14), 3208–3211 (2018).
5. P. Cheben, J. Čtyroký, J. H. Schmid, *et al.*, "Bragg filter bandwidth engineering in subwavelength grating metamaterial waveguides," Opt. Lett. **44**(4), 1043–1046 (2019).
6. D. Pereira-Martín, J. M. Luque-González, J. G. Wangüemert-Pérez, *et al.*, "Complex spectral filters in silicon waveguides based on cladding-modulated Bragg gratings," Opt. Express **29**(11), 15867–15881 (2021).
7. W. Zhang and J. Yao, "A fully reconfigurable waveguide Bragg grating for programmable photonic signal processing," Nat. Commun. **9**(1), 1396 (2018).
8. A. D'Orazio, M. D. Sario, V. Petruzzelli, *et al.*, "Photonic band gap filter for wavelength division multiplexer," Opt. Express **11**(3), 230–239 (2003).
9. E. Luan, H. Shoman, D. M. Ratner, *et al.*, "Silicon photonic biosensors using label-free detection," Sensors **18**(10), 3519 (2018).

Optics EXPRESS

10. J. M. Luque-González, A. Sánchez-Postigo, A. Hadij-ElHouati, *et al.*, "A review of silicon subwavelength gratings: building break-through devices with anisotropic metamaterials," Nanophotonics **10**(11), 2765–2797 (2021).
11. H. Altug, S.-H. Oh, S. A. Maier, *et al.*, "Advances and applications of nanophotonic biosensors," Nat. Nanotechnol. **17**(1), 5–16 (2022).
12. S. Arshavsky-Graham, N. Massad-Ivanir, E. Segal, *et al.*, "Porous silicon-based photonic biosensors: Current status and emerging applications," Anal. Chem. **91**(1), 441–467 (2019).
13. E. Luan, H. Yun, M. Ma, *et al.*, "Label-free biosensing with a multi-box sub-wavelength phase-shifted Bragg grating waveguide," Biomed. Opt. Express **10**(9), 4825–4838 (2019).
14. M. Soler, O. Calvo-Lozano, M.-C. Estevez, *et al.*, "Nanophotonic biosensors: Driving personalized medicine," Opt. Photonics News **31**(4), 24–31 (2020).
15. J. Jágerská, H. Zhang, Z. Diao, *et al.*, "Refractive index sensing with an air-slot photonic crystal nanocavity," Opt. Lett. **35**(15), 2523–2525 (2010).
16. G. M. Paternó, G. Manfredi, F. Scotognella, *et al.*, "Distributed Bragg reflectors for the colorimetric detection of bacterial contaminants and pollutants for food quality control," APL Photonics **5**(8), 080901 (2020).
17. J. G. Wangüemert-Pérez, A. Hadij-ElHouati, A. Sánchez-Postigo, *et al.*, "Subwavelength structures for silicon photonics biosensing," Opt. Laser Technol. **109**, 437–448 (2019).
18. L. Torrijos-Morán, A. Griol, and J. García-Rupérez, "Experimental study of subwavelength grating bimodal waveguides as ultrasensitive interferometric sensors," Opt. Lett. **44**(19), 4702–4705 (2019).
19. M. Odeh, K. Twayana, K. Sloyan, *et al.*, "Mode sensitivity analysis of subwavelength grating slot waveguides," IEEE Photonics J. **11**(5), 1–10 (2019).
20. C. Pérez-Armenta, A. Ortega-Mo nux, J. Čtyrokỳ, *et al.*, "Narrowband Bragg filters based on subwavelength grating waveguides for silicon photonic sensing," Opt. Express **28**(25), 37971–37985 (2020).
21. J. G. Wangüemert-Pérez, P. Cheben, A. Ortega-Mo nux, C. Alonso-Ramos, D. Pérez-Galacho, R. Halir, I. Molina-Fernández, D.-X. Xu, and J. H. Schmid, "Evanescent field waveguide sensing with subwavelength grating structures in silicon-on-insulator," Opt. Lett. **39**(15), 4442–4445 (2014).
22. S. Heinsalu, Y. Isogai, Y. Matsushima, *et al.*, "Record-high sensitivity compact multi-slot sub-wavelength Bragg grating refractive index sensor on SOI platform," Opt. Express **28**(19), 28126–28139 (2020).
23. P. Xu, J. Zheng, J. Zhou, *et al.*, "Multi-slot photonic crystal cavities for high-sensitivity refractive index sensing," Opt. Express **27**(3), 3609–3616 (2019).
24. C. Ozcan, J. S. Aitchison, and M. Mojahedi, "Optimization of bulk sensitivity for strip, slot, and subwavelength grating-based waveguides for dual-polarization operation," Opt. Express **31**(3), 3579–3594 (2023).
25. X. Wang, J. Flueckiger, S. Schmidt, *et al.*, "A silicon photonic biosensor using phase-shifted Bragg gratings in slot waveguide," J. Biophotonics **6**, 821–828 (2013).
26. D. M. Kita, J. Michon, S. G. Johnson, *et al.*, "Are slot and sub-wavelength grating waveguides better than strip waveguides for sensing?" Optica **5**(9), 1046–1054 (2018).
27. H. Yan, L. Huang, X. Xu, *et al.*, "Unique surface sensing property and enhanced sensitivity in microring resonator biosensors based on subwavelength grating waveguides," Opt. Express **24**(26), 29724–29733 (2016).
28. J. Flueckiger, S. Schmidt, V. Donzella, *et al.*, "Sub-wavelength grating for enhanced ring resonator biosensor," Opt. express **24**(14), 15672–15686 (2016).
29. L. Chrostowski, S. Grist, J. Flueckiger, *et al.*, "Silicon photonic resonator sensors and devices," Proc. SPIE **8236**, 823620 (2012).
30. P. Cheben, R. Halir, J. H. Schmid, *et al.*, "Subwavelength integrated photonics," Nature **560**(7720), 565–572 (2018).
31. R. Halir, A. Ortega-Monux, D. Benedikovic, *et al.*, "Subwavelength-grating metamaterial structures for silicon photonic devices," Proc. IEEE **106**(12), 2144–2157 (2018).
32. S. H. Badri and S. G. Farkoush, "Subwavelength grating waveguide filter based on cladding modulation with a phase-change material grating," Appl. Opt. **60**(10), 2803–2810 (2021).
33. S. H. Badri, "Transmission resonances in silicon subwavelength grating slot waveguide with functional host material for sensing applications," Opt. Laser Technol. **136**, 106776 (2021).
34. T. T. D. Dinh, X. Le Roux, J. Zhang, *et al.*, "Controlling the modal confinement in silicon nanophotonic waveguides through dual-metamaterial engineering," Laser Photonics Rev. **17**, 2100305 (2023).
35. S. Jahani, S. Kim, J. Atkinson, *et al.*, "Controlling evanescent waves using silicon photonic all-dielectric metamaterials for dense integration," Nat. Commun. **9**(1), 1893 (2018).
36. M. B. Mia, S. Z. Ahmed, I. Ahmed, *et al.*, "Exceptional coupling in photonic anisotropic metamaterials for extremely low waveguide crosstalk," Optica **7**(8), 881–887 (2020).
37. M. F. Kabir, M. B. Mia, I. Ahmed, *et al.*, "Anisotropic leaky-like perturbation with subwavelength gratings enables zero crosstalk," Light: Sci. Appl. **12**(1), 135 (2023).
38. X. Xu, H. Subbaraman, J. Covey, *et al.*, "Complementary metal–oxide–semiconductor compatible high efficiency subwavelength grating couplers for silicon integrated photonics," Appl. Phys. Lett. **101**(3), 031109 (2012).
39. S. Nambiar, P. Sethi, and S. K. Selvaraja, "Grating-assisted fiber to chip coupling for SOI photonic circuits," Appl. Sci. **8**(7), 1142 (2018).
40. S. Z. Ahmed, I. Ahmed, M. B. Mia, *et al.*, "Ultra-high extinction ratio polarization beam splitter with extreme skin-depth waveguide," Opt. Lett. **46**(9), 2164–2167 (2021).

Optics EXPRESS

41. M. B. Mia, S. Z. Ahmed, N. Jaidye, *et al.*, "Mode-evolution-based ultra-broadband polarization beam splitter using adiabatically tapered extreme skin-depth waveguide," Opt. Lett. **46**(18), 4490–4493 (2021).
42. Y. Xu and J. Xiao, "Compact and high extinction ratio polarization beam splitter using subwavelength grating couplers," Opt. Lett. **41**(4), 773–776 (2016).
43. M. B. Mia, N. Jaidye, I. Ahmed, *et al.*, "Broadband integrated polarization splitter and rotator using subwavelength grating claddings," Opt. Express **31**(3), 4140–4151 (2023).
44. Y. Xiong, J. G. Wangüemert-Pérez, D.-X. Xu, *et al.*, "Polarization splitter and rotator with subwavelength grating for enhanced fabrication tolerance," Opt. Lett. **39**(24), 6931–6934 (2014).
45. I. Ahmed, S. Z. Ahmed, N. Jaidye, *et al.*, "High-density integrated delay line using extreme skin-depth subwavelength grating waveguides," Opt. Lett. **48**(7), 1662–1665 (2023).
46. J. Wang, R. Ashrafi, R. Adams, *et al.*, "Subwavelength grating enabled on-chip ultra-compact optical true time delay line," Sci. Rep. **6**(1), 30235 (2016).
47. S. H. Badri and M. M. Gilarlue, "Silicon nitride waveguide devices based on gradient-index lenses implemented by subwavelength silicon grating metamaterials," Appl. Opt. **59**(17), 5269–5275 (2020).
48. J. M. Luque-González, R. Halir, J. G. Wangüemert-Pérez, *et al.*, "An ultracompact GRIN-lens-based spot size converter using subwavelength grating metamaterials," Laser Photonics Rev. **13**, 1900172 (2019).
49. K. E. Zinoviev, A. B. González-Guerrero, C. Domínguez, *et al.*, "Integrated bimodal waveguide interferometric biosensor for label-free analysis," J. Lightwave Technol. **29**(13), 1926–1930 (2011).
50. D. Pimbi, M. Hasan, M. B. Mia, *et al.*, "Polarization-independent photonic Bragg grating filter with cladding asymmetry," Opt. Lett. **48**(5), 1192–1195 (2023).
51. D. Dai, L. Liu, S. Gao, *et al.*, "Polarization management for silicon photonic integrated circuits," Laser Photonics Rev. **7**, 303–328 (2013).
52. H. Okayama, Y. Onawa, D. Shimura, *et al.*, "Polarisation-independent wavelength filter using Si wire waveguide Bragg grating and multimode interference couplers," Electron. Lett. **50**, 388–389 (2014).
53. M. Roussey, P. Stenberg, A. Bera, *et al.*, "Polarization independent integrated filter based on a cross-slot waveguide," Opt. Express **22**(20), 24149–24159 (2014).
54. H. Sun and L. R. Chen, "Polarization independent Bragg gratings using tilted subwavelength grating waveguide Bragg gratings," Opt. Express **31**(2), 1214–1223 (2023).
55. B. Tabti, F. Nabki, and M. Ménard, "Polarization insensitive Bragg gratings in Si_3N_4 waveguides," in *Advanced Photonics 2017 (IPR, NOMA, Sensors, Networks, SPPCom, PS)*, (Optica Publishing Group, 2017), p. IW2A.5.
56. H. Okayama, Y. Onawa, D. Shimura, *et al.*, "Polarization rotation Bragg grating using Si wire waveguide with non-vertical sidewall," Opt. Express **22**(25), 31371–31378 (2014).
57. H. Yun, Z. Chen, Y. Wang, *et al.*, "Polarization-rotating, Bragg-grating filters on silicon-on-insulator strip waveguides using asymmetric periodic corner corrugations," Opt. Lett. **40**(23), 5578–5581 (2015).
58. D. Pimbi, M. Hasan, M. B. Mia, N. Jaidye, and S. Kim, "Photonic Bragg gratings with cladding asymmetry for polarization independent and rotation filter," in *CLEO 2023*, (Optica Publishing Group, 2023), p. JW2A.112.
59. Ansys ®Academic Lumerical Research, Release 2021 R2, https://www.ansys.com.
60. M. van Niekerk, S. Jahani, J. Bickford, *et al.*, "Two-dimensional extreme skin depth engineering for CMOS photonics," J. Opt. Soc. Am. B **38**(4), 1307–1316 (2021).